Microwave-assisted synthesis of reduced graphene oxide and vanadium pentoxide hybrid materials for enhanced performance in next generation batteries

by

Levon Aldon LeBan II

B.S., Xavier University of Louisiana, 2017

A THESIS

submitted in partial fulfillment of the requirements for the degree

MASTER OF SCIENCE

Department of Chemistry
College of Arts and Sciences

KANSAS STATE UNIVERSITY
Manhattan, Kansas

2020

Approved by:

Major Professor
Dr. Jun Li

Copyright

Abstract

In a world of increasing energy demands, the need for possible alternatives to lithium in electrical energy storage systems (EES) grows. This opens up the door to the utilization of divalent ion systems (Zn^{2+} and Mg^{2+}). Magnesium has the specific advantage of possessing high abundance in the earth's crust (2.1%), higher volumetric capacity (3833 mAh/cm^3 vs. 2046 mAh/cm^3), and safer operation due to the lack of dendrite formation during cycling. Zinc also possesses a higher volumetric capacity (5854 mAh/cm^3 vs 2046 mAh/cm^3), and can be constructed using aqueous electrolytes. The divalent nature of magnesium & zinc ions is also a disadvantage, as ions diffuse significantly more slowly than lithium ions. Hydrated V_2O_5 is expected to help address this issue due to its open structure and large interlayer distance. In addition, water within the crystal structure helps to shield the positive charge of divalent ions as they diffuse into the host material. The low V_2O_5 conductivity can be improved via forming a hybrid material with a conductive carbon template. This was achieved using microwave-assisted synthesis with the vanadium (V) oxytrisisopropoxide (VTIP), H_2O, and graphene oxide (GO) to create a hybrid structure of hydrated V_2O_5 on the reduced graphene oxide (rGO). Microwave-assisted synthesis enables fast specific heating, reaching an elevated temperature (180 C˚) and pressure (15 bar) similar to a hydrothermal reaction. This was followed by an annealing step that allows for controlling the degree of hydrations and study its effect on the electrochemical performance. Materials characterization using thermogravimetric analysis (TGA), Raman spectroscopy, scanning electron microscopy (SEM), x-ray diffraction (XRD), X-ray photo electron spectroscopy (XPS) and transmission electron microscopy (TEM) has revealed that the hydrated V_2O_5 has been successfully deposited on the rGO surface, forming a strongly attached hybrid material. Electrochemical tests show that the material can function as a cathode for 2 and 3 lithium insertion,

at C/9, C/6, C/3 and C rates, achieving the theoretical capacity (294 mAh/g for 2 Li^+ processes) at C/9 and maintaining a good coulombic efficiency (>98%). Increasing the current rate in this and all subsequent cell conditions decreases the capacity. The initial magnesium cells are found to perform poorly, suffering from the poor stability and low reversibility, mainly limited by the low Mg^{2+} ion conductivity across the compact solid electrolyte interface (SEI). By preforming a lithium-salt-containing SEI layer in a Li-ion battery and then using it as the magnesium anode was found to overcome the limitation by the Mg anode and allow the observation of the properties of the cathode based on the hybrid material. Magnesium insertion at C/8, C/4, C/2, and C rate exhibits a peak capacity of 165 mAh/g (0.56 moles Mg insertion) at C/8 and maintains good coulombic efficiency (~95%). The material shows promise for Zinc ion cells, at C, 2C, 4C, and 8C, achieving a high capacity of 410 mAh/g (1.39 moles Zn insertion) at 1C while maintaining a high coulombic efficiency (>98%).

Table of Contents

List of Figures

long cycling measurement of the 350 ˚C annealed sample using a polished magnesium electrode at C/2.

Figure 12. (a-c) Three rate performance cycles of the As-synthesized, 220, and 350 ˚C annealed condition using a SEI treated magnesium counter electrode at C/8, C/4, C/2, C.

Figure 13. (a-c) Cyclic Voltammograms of all three conditions in a zinc ion cell at 1, 0.8, 0.5, and 0.2 mV/s

Figure 14.. (a) Three rate performance cycles of the As-synthesized, 220 ˚C and 350 ˚C annealed samples versus a Zinc anode at C, 2C, 4C, 8C. (Current densities: 200,400, 800, 1600 mA g^{-1}) (b) Three long term cycling of the as-synthesized, 220 ˚C and 350 ˚C annealed samples versus a Zinc anode at 1C rate. (c-e) Three long cycling tests of the as-synthesized, 220 ˚C and 350 ˚C annealed samples versus a Zinc anode at 4C in comparison to 1C rates.

List of Tables

Acknowledgements

I’d like to acknowledge Dr. Jun Li, Dr. James Emory Brown, Dr. Ya Chen, Dr. Dan Boyle, Kamalambika Muthukumar, the rest of the Li group, and the reading committee for your support.

Chapter 1 - Introduction

Global demand for energy has increased manifold as more of the developing world continues to industrialize. In fact, the U.S. Energy Information Administration projects global energy consumption will increase 50% within the next 3 decades, the largest fraction of that usage coming from industrial and transportation applications. Unfortunately, recent increases in energy production have been driven by fossil fuels, which only serve to further exacerbate the climate crisis. A prominent example is the tonnage of carbon per capita will increase to 6.6 million tons of carbon dioxide per capita by 2030.[1] Relying on renewable energy sources such as solar, wind, geothermal, hydroelectric etc. will be paramount to a sustainable future, but this will require greatly expanding the use of battery-based energy storage systems. Energy storage systems currently used are only capable of storing 1% of the energy generated.[1, 2] While lithium storage systems, i.e. Li-ion batteries (LIBs), have high specific energy (150-200 Wh/kg) and have achieved great success in personal devices, they are insufficient for wider scale grid and transportation use.[1, 3] One of the biggest obstacles for the adoption of lithium ion batteries is cost. A prominent example is an electric car battery pack that costs \$500 kWh^{-1} on average.[4] Lithium's high cost is driven by demand plus its scarcity in the earth's crust (0.002%). According to the 2020 report by the United States Geological Survey the price of battery grade lithium in 2018 was \$17000 per ton. In addition to the cost issues, the flammability of organic electrolytes, the high energy cost of LIB manufacture, and the lack of abundance of LIB components. However, this opens up a space for the application of divalent ion systems for grid-based storage.[1, 3-5]

Divalent ion systems have 3 advantages over more conventional lithium systems for grid and transportation infrastructure. The first is an increased abundance in the earth's crust, and a lower cost per ton, especially when comparing the cost of lithium to magnesium, zinc, and calcium

($ 17500 vs 4500, 2380, 2250 per ton). Another reason is that the incorporation of aqueous components makes divalent system electrolytes less flammable and more environmentally friendly in comparison to the electrolytes used in lithium ion systems. In addition, lithium anodes are unusable in commercial rechargeable cells, due to the lack of electrode stability and the formation of dendrites during cycling, which can cause safety issues.[6] The last reason is that the specific volumetric capacity of divalent ions is higher than that of lithium ion systems, making them more suitable for grid and transportation applications.[7] For example, magnesium-ion technology is promising specifically because its abundance in the earth's crust is 10^4 times of that of lithium and magnesium is more stable in atmosphere, making it safer relative to lithium.[8] The divalent nature of magnesium ions also presents a potential advantage in terms of volumetric capacity (3833 mAh/cm^3 for Mg vs. 2046 mAh/cm^3 for Li). Zinc ion batteries can have high capacity (820 mAh g^{-1}) and good compatibility with aqueous solvents.[9]

Despite the apparent advantages, divalent ion batteries are seriously hindered due to a plethora of challenges. One challenge is lack of high-capacity cathode materials with an adequate operating voltage.[7-9] Another, perhaps greater issue is that divalent ions intercalation /deintercalation have sluggish ion diffusion due to the increased electrostatic attraction and the redistribution of cations within the host material. Magnesium ion batteries specifically suffer from the formation of a film, i.e. solid electrolyte interphase (SEI), on the magnesium metal surface that blocks the transport of Mg^{2+} ions.[8, 10] The use of magnesium salts such as $Mg(ClO_4)_2$ and $Mg(BF_4)_2$ paired with organic solvents result in the formation of surface films which passivate the magnesium metal electrode.[7, 9] A specific issue with zinc ion systems is the poor stability of electrode materials upon the introduction of guest species.[9] Designing divalent ion systems will require both a suitable cathode material that that can reversibly intercalate divalent ions in addition

to a method to increase the diffusion rate of the ions. One method of increasing diffusion rates is the inclusion of water into the cathode material's crystal structure.[8, 11] Water in a hydrated electrode material or electrolyte, can effectively screen electrostatic divalent ion interactions and serve as a lubricant for the divalent ions.[11] V_2O_5 is a good candidate for cathode material because it can host reversible intercalation/deintercalation of divalent ions, has a tunable interlayer spacing and a tunable degree of hydration that can be altered via controlling the annealing temperature.[2, 12, 13] V_2O_5 is also desirable because it can achieve high theoretical capacities (294 mAh g^{-1}) and nanostructured V_2O_5 has tunable morphology that can enhance the electrode transport kinetics.[6] When attached to the rGO template, the hydrated V_2O_5 combines high capacity and enhanced diffusion kinetics with the high stability and conductivity of rGO.

In this thesis research my foci are to synthesize a hybrid material of hydrated V_2O_5 and rGO using microwave synthesis and test its efficacy in lithium, magnesium, and zinc ion batteries. This thesis will cover the reason why microwave synthesis was utilized and its role in crafting the hybrid material. Materials characterization will cover the following techniques, Raman, XRD, SEM, TEM, and XPS in order understand the synthesized materials. Finally, the material will be used as a cathode material that is coupled with lithium, magnesium and zinc anodes for battery tests in coin cells. Each cell is characterized with electrochemical techniques including cyclic voltammetry, galvanostatic charge-discharge at different rates and long-term cycling, in order to evaluate its viability as a next generation battery material.

Chapter 2 - Methods

Hydrated V_2O_5, while a viable cathode material suffers from poor conductivity due to its band gap of 2.2 eV rendering it a semiconductor. The main method to mitigate this drawback is via the introduction of a conductive (10^{2}-10^{3} Ω^{-1} m^{-1}) and mechanically robust reduced graphene oxide (rGO) template.[14] The introduction of the rGO template also provides control over the morphology, composition and microstructure of the deposited V_2O_5.[11, 15] To synthesize V_2O_5, vanadium isotrisoxypropoxide (VTIP) precursor is utilized, which hydrolyses into V_2O_5. Compared to ammonium metavanadate used in other studies, VTIP is more effective to form evenly distributed oxide domains on the rGO template.[16] GO is used instead of rGO directly because it is easier to be dispersed in an organic solvent like tetra-hydrofuran (THF).[17] THF is used as the primary solvent due to its microwave transparency and its ability have GO and VTIP dispersed in solution.

Synthesis Detail

The main approach to synthesizing the V_2O_5-rGO hybrid material was to utilize microwave synthesis. The main advantage of microwave synthesis is that solvothermal conditions can be achieved much faster than most hydrothermal reactions, taking up to thirty minutes while hydrothermal reactions can take many hours, enabling the testing of a wide variety of experimental conditions.[18] When utilizing microwave synthesis, a materials tangent loss value must be taken into account. [19] The tangent loss quantifies a dielectric materials' inherent dissipation of electromagnetic energy.[20, 21] The lower the tangent loss value, the more microwave transparent the material is. The graphene

Table 1. Loss tangent (tanδ) values (at 2.45 GHz and 20° C)

Material	Tangent Loss value
V_2O_5	< 0.1
GO	0.9-1.5
THF	0.042
Water	0.123

oxide (GO), utilized as a precursor, has the highest tangent loss value within the reaction mixture, meaning that its rapid heating causes vanadium isotrisoxypropoxide (VTIP) to convert into V_2O_5 as the high pressure and temperature of the microwave strip away GO' oxygen groups, turning it into rGO. [22] The reaction mixture was prepared first, by dispersing 30% weight of graphene oxide (GO) within 25ml of tetrahydrofuran (THF) using ultrasonication. Once the GO was dispersed within the solution, 62 microliters of vanadium isotrisoxypropoxide (VTIP) and 0.32 ml of water added to the dispersed solution to hydrolyze the VTIP. The VTIP-GO mixture is left to hydrolyze for 2 hours. Once the mixture is hydrolyzed, it is placed in the microwave within the Jun Li laboratory (Discover SP, CEM, Matthews, NC), set to 180 ˚C for 30 min at an applied power of 300 watts, reaching a pressure of 8 bar. This triggered a solvothermal reaction converting the VTIP to V_2O_5 on top of the GO surface as the GO converted into reduced graphene oxide (rGO). Once the product was removed from the microwave it was transferred to a 50 ml plastic tube and centrifuged. The solvent was then dried overnight at 85 degrees. In order to control the degree of hydration portions of the product were annealed within a tube furnace in air for 2 hours at 220 C and 350 C respectively, in order to create a fully hydrated ($1.6H_2O$), partially hydrated ($0.54H_2O$), and fully dehydrated ($0.30H_2O$) versions of the product. Varying the hydration allows for the evaluation of water's effect on the morphology and electrochemical performance.

Materials Characterization

Once the hybrid product is synthesized, thermogravimetric analysis (TGA), Raman spectroscopy, scanning electron microscopy (SEM), transmission electron microscopy (TEM), X-ray diffraction (XRD) and X-ray Photoelectron Spectroscopy (XPS) are the primary means of materials characterization. Thermal gravimetric analysis (TGA) was carried out from room temperature to 700 °C under a dynamic compressed air atmosphere at a heating rate of 10 °C min-

[1] using a Pyris 1 TGA system (PerkinElmer, USA) in Prof. Aakeroy's laboratory. TGA gives information on the percent composition of V_2O_5, rGO and degree of hydration. TGA was executed using an atmosphere of compressed air from the temperature range of 25-700 ˚C. In this temperature range all adsorbed and crystalline water vanishes, GO converts to rGO, and rGO thermally decomposes, all in distinct phases while the weight of V_2O_5 largely remains constant within the material. A consequence of preforming the measurement in air is that in order to calculate the percent weight of carbon in the hybrid material, a graphene oxide reference was required. Raman spectroscopy can help to determine two things; first, whether vanadium oxide material was present in the hybrid material, and second, the quality of rGO in the hybrid material. All Raman spectra were obtained with a laser with an excitation wavelength of 532 nm at a 1 cm^{-1} resolution grating using a DXR Raman microscope (Thermo Scientific, Waltham, MA, US) in the Jun Li laboratory. The Raman shift range examined in the Raman spectra was 80 cm^{-1} to 3,000 cm^{-1}. This range is ideal for picking up the characteristic vanadium oxide peaks between 80-1250 cm^{-1} and the characteristic rGO peaks that lay at 1360, 1582, and 2700 cm^{-1} respectively. In order to maximize the signal to noise ratio the slit width was set to 50 micrometers, while the laser power was set to 10 mW. The SEM and TEM imaging are used to ascertain the morphology and average particle size of the hybrid materials. Using Field Emission Scanning Electron Microscope (SEM) (Topcon/ISI/ABT DS 130F) in the Jun Li Laboratory at 3.5 kV and magnifications between 5k and 10k, low-magnification morphology of the hybrid material was observed. Higher-magnification images were obtained using a TEM (CM-100, FEI company, Hillsboro, Oregon, US) in the microscope facility of the Division of Biology at Kansas State University. All TEM images were created via depositing a drop of diluted suspension on a carbon film-coated copper grid. TEM measurements were performed at 100kV at the magnifications of 34,000X and

130,000X to achieve full image scales down to 200 and 50 nm respectively. This allowed for a more in-depth evaluation of particle size. X-ray diffraction spectra (XRD) can reveal the products' interlayer spacing and its crystallinity. XRD spectra were obtained through a D8 ADVANCE diffractometer (Bruker, Germany) within the Chemistry Department using Cu Kα (1.5406 Å) radiation and a 2 mm slit width. The 2-theta range utilized for the as-synthesized product was ~ 5 to 40˚ for two reasons. The first one is that the range was enough to identify the bilayer V_2O_5 peak which can appear between 5-12˚ in 2theta angle. The second reason was to shorten the 2theta range so that the low signal to noise ratio could be improved by increasing the materials' exposure time. As the annealing condition at 220 ˚C was more crystalline and had higher signal to noise, the spectra was stopped at 60˚ 2theta angle. There were no relevant V_2O_5 peaks past that point. The 2theta range was used for the annealing condition at 350 ˚C is 5-60˚ 2theta angles, as it matched commercial and crystalline alpha-V_2O_5. XPS was done using a K-Alpha XPS system (Thermo Fisher, Waltham, MA, US) using Al Ka radiation with an energy of 1,486.6 eV in the Nanoscale facility at the University of Nebraska-Lincoln. The binding energy range utilized was between 540-510 eV which captures both V2p peaks in the 515-527 eV range, but the O1s peak also resided between 527 and 540 eV. The peaks were fitted using Origin's peak fitting program to find the atomic percentages of the various species based on the fitted peak area and corresponding sensitivity factors provided by the facility.

Electrochemical Characterization

For electrochemical tests, V_2O_5-rGO hybrid electrodes were fabricated by coating an n-methyl-2-pyrrolidone (NMP) (Fisher Scientific, Pittsburg, PN, US) based slurry with a mixture of 85 wt % of active materials, 10 wt % of super P carbon black (Alfa Aesar, Ward Hill, MA, USA), and 5 wt % of poly(vinylidene fluoride-hexafluoropropylene) (PVdF-HFP, MW = 40 000) binder

onto a current collector. For lithium and magnesium cells the active material was deposited onto a 15-micrometer thick aluminum foil coated with 4 micrometers of carbon (MTI, Richmond, California, US). The coating was done using a (MTI) film coater which deposits ~1 mg/cm^2 of material on the aluminum foil. The foil was punched into a 15-millimeter disks which when coated are roughly 0.1 mm thick. For zinc cells the slurry was coated onto 15-micrometer thick titanium foil using a paint brush, coating approximately ~1.5 mg/cm^2 of material onto to the foil, leaving the final coated electrode approximately 0.1 mm thick.

For LIB and MIB cathode tests, the electrodes were assembled into CR2016 coin cells (MTI, Richmond, CA, US) in an Ar-filled glovebox (LabStar50, MBraun, Garching, Germany) with <0.5 ppm of H_2O and <0.5 ppm of O_2. A lithium foil disc of 0.1 mm thickness and 15 mm in diameter (MTI, Richmond, CA, US) was used as the counter electrode. A borosilicate electrolyte-soaked fiberglass (El-cells, Hamburg, Germany) served as the separator. An electrolyte solution of 1.0 M lithium hexafluorophosphate ($LiPF_6$) in a mixture of ethylene carbonate (EC), ethyl methyl carbonate (EMC) and dimethyl carbonate (DMC) (1:1:1 v/v) plus 2% vinylene carbonate

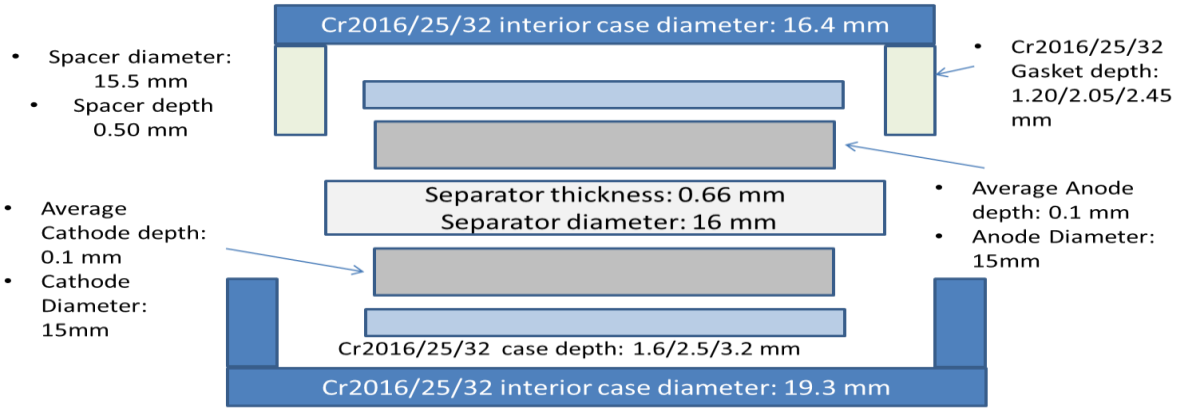

Figure 1. A diagram depicting the interior of the coin cells used in all electrochemical testing.

(Novolyte, Cleveland, OH, USA) was used. The cell performance such as charge–discharge capacity at varied C-rates (a rate of 1C corresponding to completing charge or discharge in 1 h),

galvanostatic charge–discharge curves, and long-cycling stability in a voltage range of 2.0–4.0 V (versus Li^+/Li) was examined using a 24-channel battery analyzer (Neware, Shenzhen, China). Electrochemical data for this and all subsequent battery tests were collected in a two-electrode system by cyclic voltammetry (CV) using an electrochemical workstation (Ivium, Eindhoven, The Netherlands).

For MIB cathode tests, a mechanically polished magnesium foil was used as the counter electrode and an electrolyte-soaked fiberglass as the separator. An electrolyte solution of 1.0 M Magnesium Perchlorate ($MgClO_4$) in a dehydrated Acetonitrile solvent was used. The cell performance such as charge–discharge capacity at varied C-rates (a rate of 1C corresponding to completing charge or discharge in 1 h) and long-cycling stability under a voltage range of 0.1–3.0 V (versus Mg/Mg^{2+}) was examined using a 24-channel battery analyzer (Neware, Shenzhen, China). Electrochemical data was collected in a two-electrode system by CV and galvanostatic charge–discharge using an Ivium,10 channel system (Invium Eindhoven, The Netherlands). When attempting to engineer the magnesium SEI layer, polished magnesium served first as the working electrode for lithium cells utilizing an electrolyte 1.0 M lithium hexafluorophosphate ($LiPF_6$) in a mixture of ethylene carbonate (EC), ethyl methyl carbonate (EMC) and dimethyl carbonate (DMC) (1:1:1 v/v) plus 2% vinylene carbonate (Novolyte, Cleveland, OH, USA) and a lithium anode. The Mg/Li cell was cycled four times at a potential range of 0.1- 1.6 V (versus Li/Li^+) for in order to deposit lithium SEI on the magnesium surface using CV in the 10 channel Ivium (Ivium, Eindhoven, The Netherlands), before the cell was dissembled and the Li-SEI covered magnesium was used as the anode in a coin cell with a V_2O_5-rGO cathode.

For ZIB cathode tests, the electrodes were assembled into CR2016 coin cells in air. Zinc foil was used as the counter electrode and an electrolyte-soaked fiberglass as the separator. A

solution of 2.0 M zinc perchlorate ($Zn(ClO_4)_2$) in aqueous solution was used as the electrolyte. The cell performance such as charge–discharge capacity at varied C-rates (a rate of 1C corresponding to completing charge or discharge in 1 h) and long-cycling stability under a voltage range of 0.2–1.8 V (versus Zn^{2+}/Zn) was collected using the 24-channel battery analyzer described above. Electrochemical data were collected in a two-electrode system by CV and galvanostatic charge–discharge using a CHI 760D electrochemical workstation (CH Instruments, Austin, TX).

Chapter 3 - Materials Characterization

Raman Spectra

Raman spectra of the as-synthesized and annealed products in Figure 2a show that the hybrid material possesses the typical peaks of V_2O_5. (405, 475, 524, 685, and 993 cm^{-1}). The peak positions are similar to those seen in commercial V_2O_5 in Figure 2c. The Raman peaks of V-O

Figure 2. (a) Raman spectra of the as-synthesized product compared to commercial V_2O_5 and bare graphene oxide. (b.) Show the I_G/I_D ratios of the rGO in each product and untreated GO. (c.) Raman spectra of the V_2O_5-rGO products at varying annealing temperatures.

(generally observed at 700 and 530 cm^{-1}) have shifted to a lower wavenumber (658-665 cm^{-1} and 485-489 cm^{-1}) for all three products with the as-synthesized product exhibiting the largest shifts and the 350 ˚C annealed condition exhibiting the smallest shifts. The shifts to lower wavenumbers are indicative of strong interaction between V_2O_5 nanoparticles and rGO sheets providing more evidence of the successful creation of a hybrid material.[18] Since the 350 ˚C product possessed the smallest shift; this sample most likely had the lowest carbon percentage. The as-synthesized product possessed a D band at 1347 cm^{-1} and a G band at 1586 cm^{-1}, while the products annealed at 220 ˚C and 350 ˚C, respectively, have D and G bands at 1350, 1352 and 1581, 1582 cm^{-1} respectively. When examining figure 2b the I_G/I_D ratio of all conditions are compared in order to evaluate the quality of rGO produced. The error bar of the I_G/I_D ratio was calculated to be +/- 0.02,

showing that the calculated differences between I_G/I_D ratios were physically meaningful. The higher the I_G/I_D, the greater the prominent the carbon sp^2 domains are within the structure and the higher the quality of rGO which leads to a higher conductivity. The as-synthesized product had an I_G/I_D ratio similar to that of commercial GO (1.11 vs 1.09) which indicates that the current synthesis conditions are insufficient at converting GO into rGO. As the annealing temperature increases so does the I_G/I_D ratio, meaning that most of the GO reduction happens during the annealing process, leaving the 220 & 350 ˚C annealed condition with the highest quality of GO (with the I_G/I_D of 1.26 vs 1.31).

Xray-Diffraction Spectra

The XRD of each sample shows how the crystallinity changes as the annealing temperature and degree of hydration change. The XRD pattern of as-synthesized hybrid V_2O_5-rGO hybrid

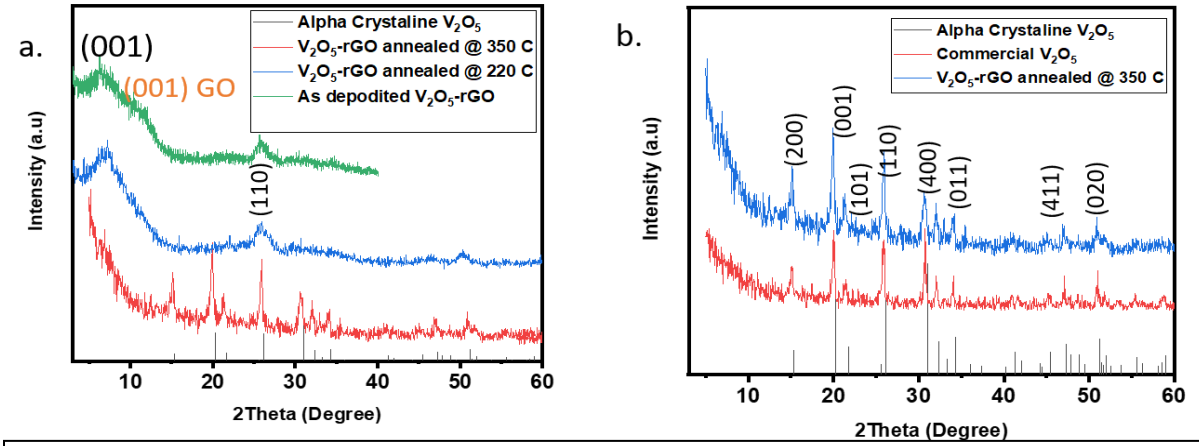

Figure 3. (a) XRD spectra of as-synthesized, 220, and 350 ˚C annealed products. (b) 350 ˚C annealed product in comparison to commercial V_2O_5.

material in Figure 3a can be attributed to the bilayer phase of V_2O_5, provided evidence that water has expanded the interlayer spacing of the V_2O_5. Based on the angle of the hydration peak ~ 6.26˚, the (001) inter layer spacing was calculated to be 14.1 Å. A second feature of the as-synthesized

product is a GO peak at 10˚ 2theta angle, which indicated that the as-synthesized product contained a high proportion of GO. The XRD spectra of the product annealed at 220 ˚C was consistent with bilayer V_2O_5, but a lower d-spacing, calculated to be 12.2 Å, indicating a lower degree of hydration within the sample. The absences of a GO peak in tandem with a higher I_G/I_D ratio support the idea that the GO was thermally reduced during the annealing process. Unlike the other two conditions, the product annealed at 350 ˚C was consistent with the JCPDS: 41-1426 databases in addition to the spectra of commercial V_2O_5 in Figure 3b. A very weak and broad diffraction peak from rGO nanosheets is observed at ~24°, which was partially overlapped with the tail of the strong (110) peak of V_2O_5. Using the Scherrer equation[29] on the (110) peak, which is present in all spectra, allow for the evaluation of crystal size which changes notably as the degree of hydration changes,

$$\tau = \frac{K * \lambda}{\beta * cos\theta} \qquad (1)$$

where K represents the shape factor, λ represents the X-ray wavelength, and β is the full width at half max.[29] Using equation (1), the as-synthesized crystal size is roughly 3.7 nm, the sample annealed at 220 ˚C yielded a crystal size of 5.1 nm, while the sample annealed at 350 ˚C yielded a crustal size of 23.3 nm. This shows a visible increase in crystal size as the degree of hydration decreases, and the crystal structure changes from bilayer to orthorhombic.

Thermogravimetric Analysis

Thermogravimetric analysis analyzed the weight percentages of rGO and V_2O_5 within the as-synthesized and annealed conditions. Since these measurements were done in an atmosphere of compressed air, a control was performed using GO treated in the microwave without the precursor. In all three conditions weight loss before 200 ˚C is believed to come from the shedding of physically adsorbed water. Examining the GO curve in Figure 4a show a massive weight loss

between 200-250 ˚C that represent the reduction of GO to rGO. Weight lost between 250- 400 ˚C is most likely from the loss of water bonded to the V_2O_5 crystal structure while weight lost after 400 ˚C is from the thermal deterioration of rGO. As V_2O_5 does not thermally destabilize until 1750 ˚C, its mass is assumed to be constant within the applied temperature range of 25-700 ˚C. The as-

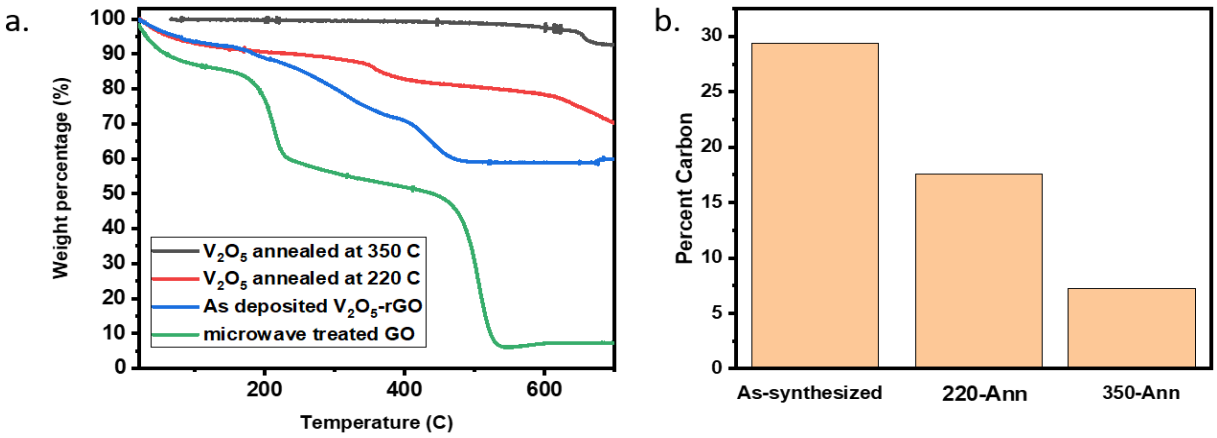

Figure 4. (a): TGA spectra of all 3 product conditions in air from room temperature to 700 ˚C compared to GO. (b) A bar graph depicting percent carbon in all samples

synthesized curve showed the highest mass loss of all three conditions between 200-400 ˚C, which when compared to the control curve, indicates that the as-synthesized sample contains both the most water of all three conditions and has the highest amount of GO. As the annealing temperature increases the weight lost between 200-400 ˚C decreases, showing a decrease in both hydration and GO. Comparing the curves of both the annealed samples show that compared to the as-synthesized sample show that much less mass is comparatively lost in the 200-400 ˚C which in conjunction with the earlier I_G/I_D ratios indicate the annealed samples contain more rGO than GO, unlike the as-synthesized sample. Figure 4b shows the calculated percentage of carbon in the hybrid material. Mass loss between 400- 600 ˚C was used to determine the percentage of carbon as the only mass loss during the range is only likely to come from carbon. When comparing the condition annealed

at 350 ˚C sample to the control GO curve the percentage of carbon is derived to be 7.21% at room temperature.

$$51.95\% - 7.27\% = (99.2 - 93.0\%) \times F_{rGO} \qquad (2)$$

F_{rGO} is the weight percentage of rGO in the starting sample (annealed V_2O_5-rGO hybrid) at the room temperature. Hence, we can derive F_{rGO} = 7.21%. Thus, the weight percentage of V_2O_5 in the hybrid is:

$$F_{V2O5\text{-}H2O} = 1 - F_{rGO} - F_{H2O} = 1 - 7.27\% = 92.73\% \qquad (3)$$

Thus, there are ~7.27% of rGO and ~92.73% of V_2O_5 in the hybrid annealed at 350 ˚C, as the annealing temperature increases the percentage of carbon within the hybrid at decreases.

X-ray Photoelectron Spectroscopy

XPS characterization supported many of the trends found in earlier materials characterization. Both Figure 5a and Figure 5d show that VTIP was not fully converted into V_2O_5

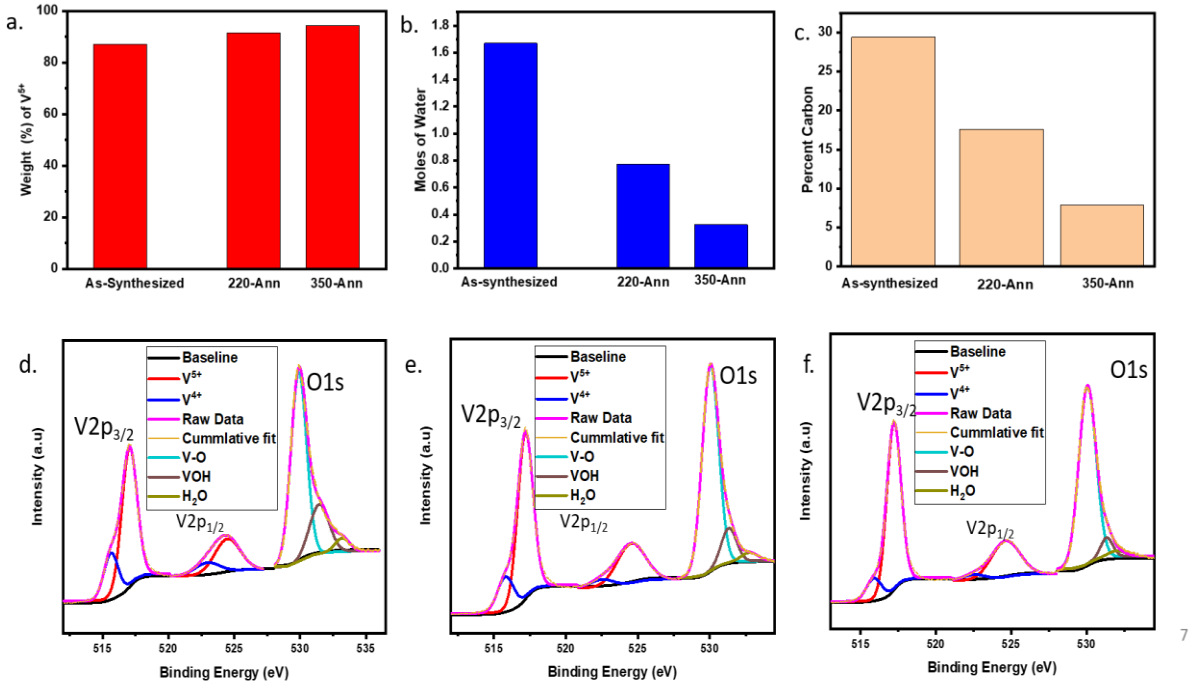

Figure 5. (a) The weight (%) of V^{5+} in each of the three conditions. (b) The moles of water in each of the three conditions. (c) The % carbon in each condition. (d-f) XPS spectra of the V2p and O1s peaks of each condition.

during the microwave-assisted synthesis, it also formed VO_2. However, as the annealing temperature increased, the proportion of VO_2 by weight decreased from 15% in the as-synthesized sample to roughly 5 wt% in the sample annealed at 350 ˚C as most of the remaining V^{4+} was oxidized under the annealing conditions. While previous characterization techniques have hinted at changes in hydration as the annealing temperature increases, XPS allows for the exact derivation of the moles of water per V_2O_5 within the structure. Figures 5a-c show that the as-synthesized sample has the most GO content at room temperature, 1.64 moles of water per mole of V_2O_5, and the highest proportion of V^{4+}. The product annealed at 220 ˚C, while it possesses more rGO, has a lower overall proportion of carbon, and has only 0.74 moles of water per V_2O_5, leaving it partially hydrated. In comparison the product annealed at 350 ˚C has the lowest amount of rGO by far in addition to being relatively dehydrated containing only 0.35 moles of water per mole of V_2O_5. Table 2 serves to reinforced trends seen in figure 5. The percentage carbon decreased as the annealing temperature increased, while the

Table 2. Displays the atomic percentage of C, O, and V in each condition

Atomic Percentage (%)	C	O	V
As-Synthesized	42.19	43.48	14.33
220 ˚C Annealed	25.25	55.70	19.05
350 ˚C Annealed	13.04	63.93	23.03

Table 3. Displays an example of the fitting parameters used in the XPS spectra, highlighting the vanadium peaks of the as-synthesized conditions.

Condition	Peak Center (eV)	Peak Height	FWHM	Area
V^{4+} 3/2p	515.64	20944.09	1.20	26789.2
V^{5+} 3/2p	517.03	68993.61	1.37	100456.2
V^{4+} 1/2p	522.83	4194.46	3.07	13394.6
V^{5+} 1/2p	523.85	17193.26	2.74	50228.1

percentage of oxygen and vanadium grew. This is reflective of the annealed samples higher proportion of V_2O_5.

Table 3 shows an example of the peak parameters used in XPS fitting specifically highlighting the as synthesized vanadium peaks. The peak parameters of peak center, peak height, full width at half max and area were left floating using the Origin's peak fitting program. The following constraints were used to ensure the fitting maintains a physical meaning. The area of 3/2p peaks must be double the area of the 1/2p peaks. The second constraint is that the 1/2p peaks must be separated from the 3/2p peaks by a minimum of 6.5 eV.[23]

SEM & TEM Imagery

The morphology of the as-synthesized V_2O_5 -rGO composite was characterized by SEM and TEM. As shown in Figures 6a, the as-synthesized V_2O_5 nanoparticles are anchored on the surface of rGO nanosheets. The V_2O_5 particles are aggregated as clusters of particles 200 nm in

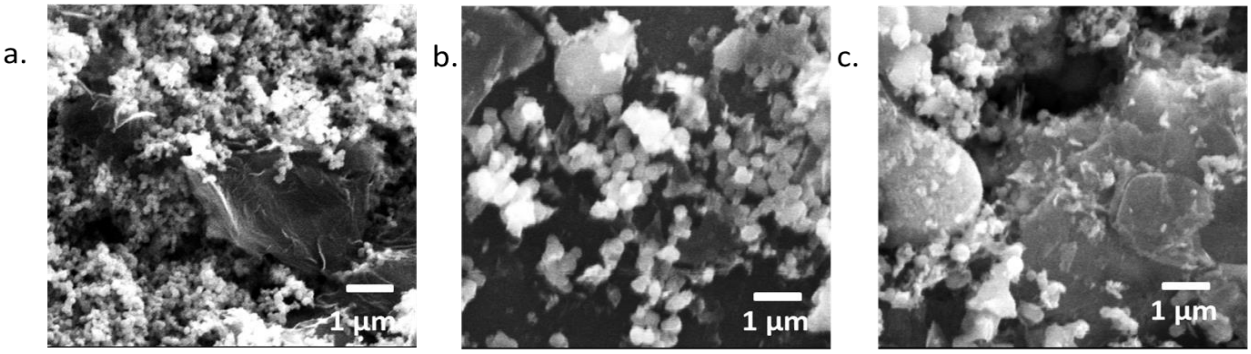

Figure 6. (a-c) SEM pictures of the As-synthesized, 220, and 350 annealed products.

diameter. Figure 6b shows the product annealed at 220 ˚C has similar aggregations of 200 nm particles on the surface of graphene plates. Noticeably the product annealed at 350 ˚C in figure 6c contains fewer aggregations of V_2O_5 particles, despite having proportionally the most V_2O_5. This suggests that most of the crystalline V_2O_5 deposited more homogenously on carbon surface as the annealing temperature increases. In both the annealed conditions, what at first appear to be flat graphene plates are shown in the TEM to be covered by a layer of smaller V_2O_5 crystals.

TEM characterization provided more detail about the morphology of each condition. All three conditions contain aggregations of V_2O_5 particles atop the graphene surface much like the SEM images. However, the 220 ˚C annealed condition in figure 7b shows a rGO plate coated with a layer V_2O_5 crystals between 5-10 nm in length, which appears to agree with the Schreier equation calculation of 5.1nm, in addition to aggregations of particles that form spheres of between 100-150 nm in diameter. The 350 ˚C annealed condition is similar to the 220 ˚C annealed condition but it shows far fewer spherical aggregations, and the orthorhombic V_2O_5 crystals that once coated the

carbon surface have expanded to between 25-75 nm in length, in addition to taking on an identifiably orthorhombic shape. When compared to the crystal sizes found using the Scherrer equation, the TEM images of the as-synthesized product don't seem consistent with the derived crystal size of 3.7 nm. This is likely to the high degree of hydration (1.64 moles of water), causing the crystals to cluster into spheroid particles that become less common in the morphology as the annealing temperature increases. The SAED patterns observed in figures 7g-i show a pattern of increasing V_2O_5 crystallinity as the annealing temperature increased and degree of hydration

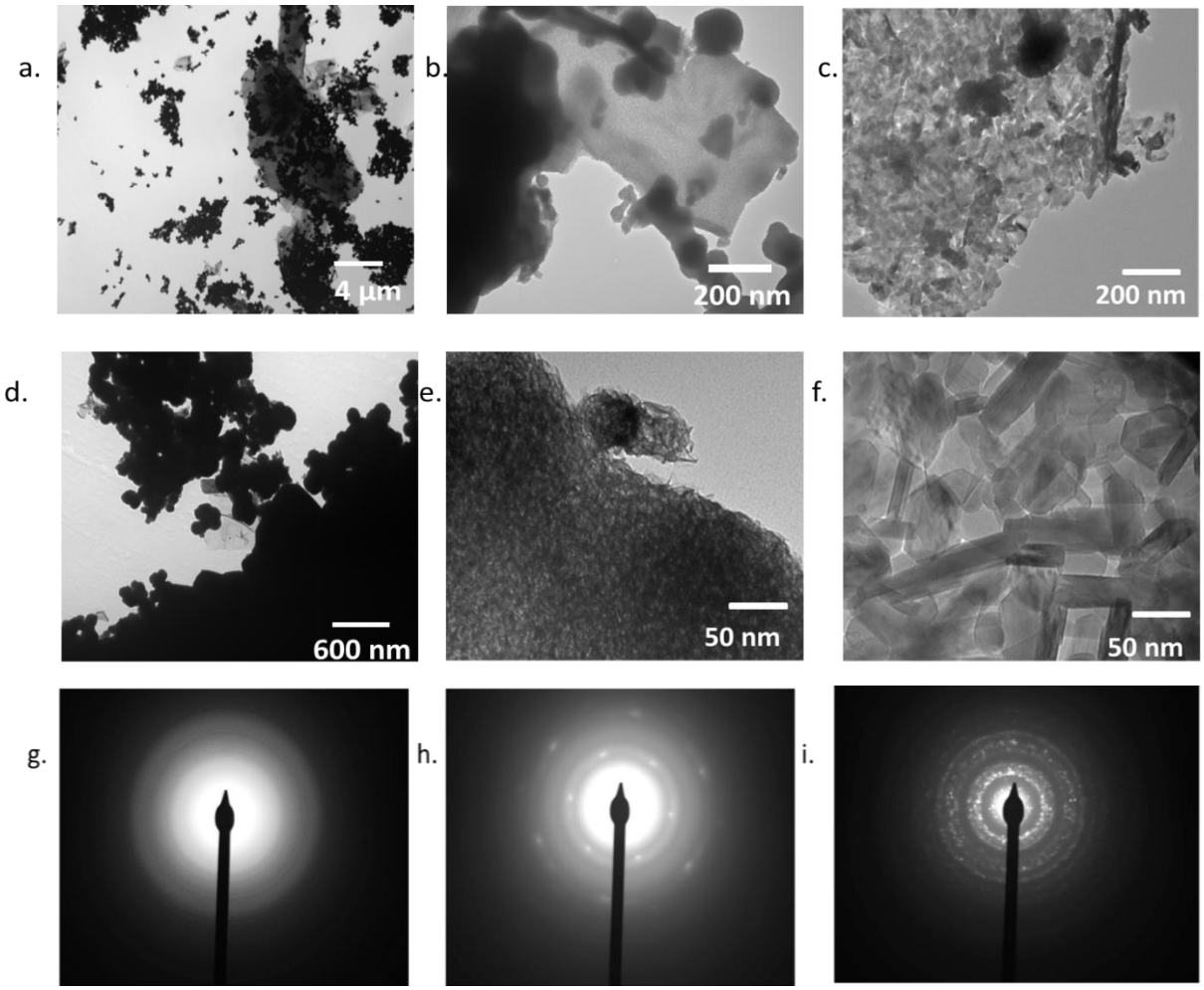

Figure 7. (a-c) Lower magnification TEM images of the three-product conditions. (d-f) Higher magnification TEM images of the three-product conditions. (g-i) Selected area electron diffraction spectra of the three-product conditions.

decreased. The SAED spectra also support the idea that the GO is reduced during the annealing process as the hexagonal pattern in figure 7h shows the representative hexagonal structure of reduced graphene oxide. This hexagonal pattern is not immediately evident in figure 7i which could be to the dense stacking of the V_2O_5 crystals, or the absence of carbon in that specific spot, as the 350 ˚C annealed condition is only 7% carbon by mass. There are two possible explanations of why rGO diffraction isn't visible. One is that the area examined possessed too thick a layer of V_2O_5, obscuring any rGO signal. Another explanation is that since the 350 ˚C annealed sample is only about 7% carbon by weight, the area examined may have had carbon that was burned out during the annealing process, leaving only V_2O_5.

Summary

Materials characterization revealed subtle changes in the material as the degree of hydration changed. The characterization so far show that the as-synthesized condition possessed the smallest crystal size and the most structural disorder, while it appeared nearly amorphous in SAED and XRD spectra. According to the XRD spectra the (001) interlayer spacing is 14.1 Å, which when combined with the other data confirms this is bi-layer V_2O_5. The degree of hydration of the as-synthesized product is 1.64 moles per mol of V_2O_5 leaving it the most hydrated condition. The as-synthesized condition had the highest proportion of carbon according to both TGA and XPS measurements (~27%), but when examining the XRD spectra the presence of a GO peak suggests that most of the GO has not been reduced in microwave. This is further supported by the low I_G/I_D ratio (1.11) seen in the Raman spectra which is comparable to that of commercial GO (1.09). In comparison, once the product was annealed at 220 ˚C the crystal size increased to 5.1 nm which is supported by the TEM imagery. The SAED and XRD indicate that the material is, like the as-synthesized condition, bi-layer V_2O_5 containing a high interlayer spacing (12.1 Å).

Unlike the as-synthesized condition its degree of hydration is only 0.74 moles of water per mole of V_2O_5, leaving it only partially hydrated. Both the XPS and TGA show that the percent carbon (7.84%) has decreased during the 2-hour annealing time, but according to the Raman spectra has a much higher percentage of rGO, due to its higher I_G/I_D ratio (1.26) and lack of GO peak in the XRD spectra. The SAED diffraction peaks also show the hexagonal crystal pattern of rGO, which is absent within the as-synthesized sample, further supporting rGO's presence in the material. Overall, the materials characterization shows that the condition annealed at 220 ˚C degrees has a higher proportion of rGO, roughly half of the hydration of the as-synthesized sample. Compared to the other two conditions the product annealed 350 ˚C is not bi-layer V_2O_5 but, more akin to alpha-crystalline V_2O_5. This is supported by the XRD spectra, which resembles commercial V_2O_5 and the dramatically reduced interlayer spacing is 4.37 Å, more comparable to the commercial alpha crystalline V_2O_5 than the other two conditions. The degree of hydration has decreased drastically compared to the other samples containing only 0.35 moles of water per mole of V_2O_5, less than a fourth of the as-synthesized samples hydration. Raman spectra indicate that the quality of rGO is similar to the 220 ˚C condition (1.26 vs 1.31), but as the XPS and TGA indicate, a far lower amount of carbon (~17% vs ~7%). Overall, we can say that the crystallinity and quality of rGO increased with annealing temperature, while the degree of hydration and % carbon weight decreasedas the annealing temperature increases.

Chapter 4 - Electrochemical Characterization

Electrochemical characterization of the V_2O_5-rGO product, serving as the working electrode, focused on measuring the voltage range, assessing the capacity delivered by each of the conditions, and measuring the stability of the conditions for lithium, magnesium, and zinc ion cells. Cyclic voltammetry measured the working electrode's potential which was measured against a reference electrode which maintains a constant potential. The current between the working electrode and counter electrode was plotted versus the applied voltage. Cyclic voltammetry helped to evaluate the applicable potential range to use in later rate performance and long-term cycling tests. Charge discharge curves showed the course of charge and discharge processes as the potential changes at a constant applied current is plotted versus time. Rate performance testing examined charge discharge cycles while the applied current density is changed. Each of the rate performance testing cycles consisted of testing four C-rates for 5 cycles each. Two important measures of performance are if the cell reaches its theoretical capacity (294.7 mAh g^{-1}) and whether the Coulombic efficiency (discharge capacity/charge capacity *100) is close to 100%. All referred C rates are based on the discharge/charge time relative to the standard rate of 1C. (corresponding to completing charge or discharge in 1 h). In all cases, the highest capacity occurs at the lowest applied current rate. How much capacity is lost from changing C-rates, and how much it recovers from moving from a high applied current to a lower one is an important measure of the reaction kinetics which defines the cell's power density and the electrode stability. Long-term cycling enabled the evaluation of the cells using a specific applied current over long cycles, typically more than fifty cycles. How much capacity is retained over the long-term cycling period is another important sign of electrode stability.

Lithium ion cell characterization

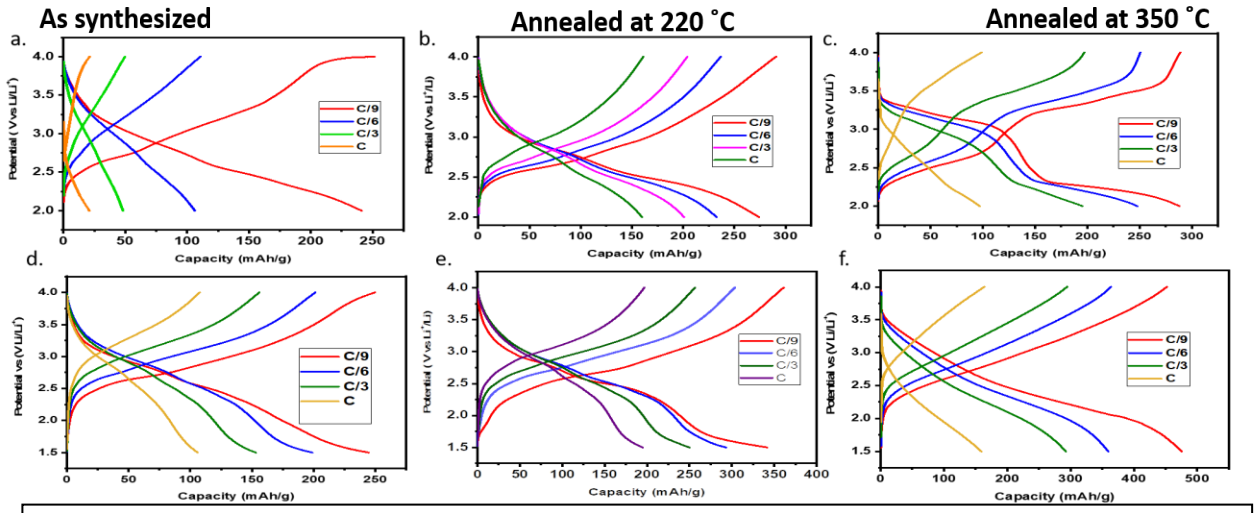

Figure 8. (a-c) Charge-discharge curves for 2 lithium insertion of the 5th cycle for each current rate for each of the three conditions. (d-f) Charge-discharge curves for 3 lithium insertion for each of the three conditions insertion of the 5th cycle for each current rate for each of the three conditions.

Figure 8 shows the charge–discharge profiles of the V_2O_5-rGO hybrid electrode in the fifth cycle at different discharge current rates, i.e. C/9, C/6, C/3, and C, respectively. The selected charge–discharge profiles presented in Figures 8a-c, represent the charge/discharge cycles of 2 lithium insertion for all three conditions in the potential range of 2- 4 V. For each condition the coulombic efficiency remained near 100% for all applied current rates indicating good electrode stability. In addition, the voltage plateaus became more prominent as the annealing temperature increased with the curve at annealing temperature of 350 ˚C displaying a voltage plateau for each lithium insertion which further shows how the crystallinity of the electrode material increased as the annealing temperature of the hybrid increases. Figures 8d-f represent the charge/discharge cycles of 3 lithium insertion for all three conditions in the potential range of 1.5- 4 V. While voltage plateaus were present in the more crystalline conditions during the 2-lithium insertion process, they are absent here due to the disruption of the crystallinity in the initial charge/discharge cycle.

It is well-known the crystalline V_2O_5 is converted into disordered materials after insertion of more than 2 Li^+ ions. However, all materials showed higher capacities when more Li^+ ions are forced to insert into the materials.

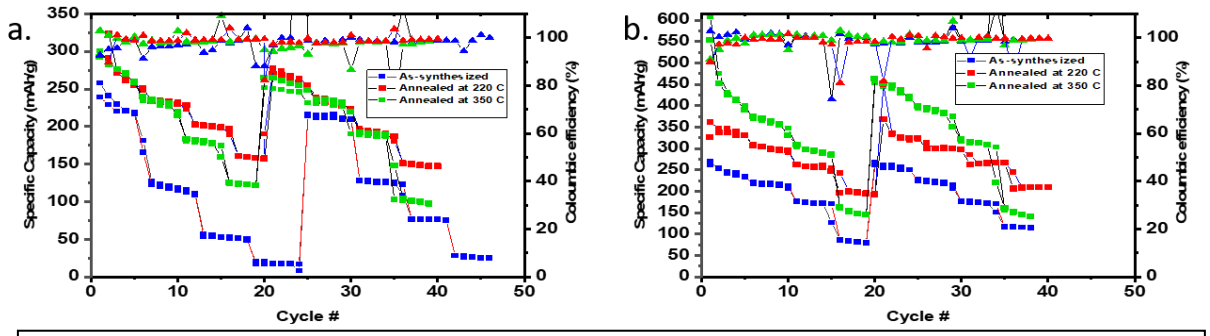

Figure 9. (a) Two rate performance cycles for 2 lithium insertion for each of the three conditions using C/9, C/6, C/3, and C.(b) Two rate performance cycles for 3 lithium insertion for each of the three conditions using C/9, C/6, C/3, and C. Current densities used were 50,75, 150, 450 ,mA g^{-1}

Figure 9a-b show the rate performance profiles of the V_2O_5-rGO hybrid electrode for 2 & 3 lithium insertion at the current rates C/9, C/6, C/3, and C. The specific capacity was calculated using the mass of the coated V_2O_5 for all three present conditions which varies from ~72% to 94% depending on the degree of hydration, based on the TGA and XPS study discussed earlier. It has been reported in the literature that the specific capacity of rGO is negligible in the voltage range between 4 and 2 V.[28] Hence, only the mass of the active material (i.e., V_2O_5) matters. For the as-synthesized condition, the first cycle, the insertion and extraction capacities reached 265 mAh g^{-1} and 248 respectively with Coulombic efficiency of ~91% at an applied C-rate of C/9 (50 mA g^{-1}). Both the annealed conditions had an initial insertion and extraction capacities reach 298 mAh g^{-1} at C/9, achieving a coulombic efficiency ~100% for both first cycle annealed conditions. The insertion/extraction capacities of the V_2O_5-rGO hybrid conditions varied with degree of hydration and apparent crystallinity. The as-synthesized sample gave capacities of 250, 128, 53 and 21 mAh

g^{-1} at C/9, C/6, C/3, and C, respectively as the columbic efficiency increased to near 100% through all the rate performance steps. After stabilizing during the first C/9 step, the capacity dropped steeply as the applied current increases. Importantly, at C/9 rate, the electrode did not reach the theoretical capacity of V_2O_5 (i.e., 294.7 mAh g^{-1}). A stable capacity of 252 mAh g^{-1} was obtained during the first C/9 rate step. After 20 cycles of rate tests, the capacity almost completely recovered to 220 mAh g^{-1} upon the second-rate performance cycle, recovering approximately 87% of the first-rate capacity. This indicates the good electrochemical stability of the V_2O_5-rGO hybrid electrode. When examining the two other annealed products in comparison with to the as-synthesized sample, they show a much higher initial capacity of 298 mAh g^{-1} that matches the theoretical capacity. The 220 ˚C annealed condition achieved stable capacities of 275, 246, 200 and 165 mAh g^{-1} at C/9, C/6, C/3, and C, respectively, as the columbic efficiency increased to near 100% through all the rate performance steps. It also showed a far lesser drop in capacity in comparison to the as-synthesized condition as the applied current increased. The 220 ˚C sample also showed a capacity retention of approximately 93% between the two rate performance cycles, indicating good electrode stability. The increased performance of the 220 ˚C annealed condition in comparison to the as-synthesized condition could be due to the fact that the as synthesized condition retained a much higher population of GO, thus does not get the conductive and stabilizing impact of rGO, which the both annealed conditions possessed according to the materials characterization. Another factor could be the V^{4+} impurity which limits the achievable capacity and lowering the energy density. Compared to the other two conditions, the product annealed at 350 ˚C had a higher specific capacity than the as-synthesized product, but the capacity decreased more than the 220 ˚C condition as the C-rate increased. In both annealed conditions, the coulombic efficiency remained near 100% after the first cycle and the capacity recovered when shifting from

a C to C/9 indicating a good overall electrode stability. The condition also possessed a capacity retention of approximately 90% between rate performance cycles. The overall superior performance of the 220 ˚C sample is most likely due to being able to take advantage of its high interlayer spacing, high degree of hydration in $V_2O_5 \cdot nH_2O$ (n = 0.74), and relatively high quality of rGO (I_G/I_D 1.27).

Examining 3-lithium insertion via expending the lower potential limit to 1.5 V showed many of the same trends as the two-lithium insertion. Like the two-lithium insertion, all three Products were measured using the applied C-rates of C/9, C/6, C/3, and C for five insertion and extraction cycles each. Expanding the lower potential limit to enable 3 lithium insertion had the least effect on the as-synthesized sample, as the C/9 capacity increased from about 250 mAh g^{-1} in the two-lithium insertion test to 275 mAh g^{-1} in the three-lithium insertion test, only a 10% improvement despite the theoretical capacity is increasing to 440 mAh g^{-1}. However, the coulombic efficiency remained at 100% for all 40 cycles, and the capacity retention between rate performance cycles was approximately 98%, indicating better electrode stability than the 2-lithium insertion condition. The insertion and extraction capacities of the 220 ˚C annealed sample stabilized at 350 mAh g^{-1} at the C/9. Upon the second-rate performance cycle, the capacity recovered back to nearly 100% of its capacity, showing excellent electrode stability when switching between current rates in addition to retaining a near 100% coulombic efficiency. While noticeably higher than the as-synthesized product, the reported 220 ˚C annealing condition's capacity was still lower than the theoretical capacity. The product annealed at 350 ˚C started with a high specific capacity of 610 mAh g^{-1} before stabilizing around 420 mAh g^{-1} within the C/9 sequence. Upon the second-rate performance cycle, the capacity recovered to roughly 450 mAh g^{-1} but decreased to 425 mAh g^{-1} at cycle 5 at C/9 rate in the second rate-sequence. While the capacity

was higher than the other two conditions, the electrode appeared to be less stable as the capacity decreased more than the other two conditions during each current step. Overall, the higher crystallinity of the alpha orthorhombic crystalline materials at 350 ˚C annealing condition allowed the capacity to reach the theoretical capacity of 440 mAh g^{-1} at C/9. In this specific situation, the degree of hydration did little to assist in the intercalation of lithium ion cells as in the 3-lithium insertion in the as-synthesized condition, indicating that the crystallinity plays a major role, especially when comparing it to the 220 ˚C condition with a similar quality of rGO.

Compared to lithium-ion battery literature, a similar mesoporous hybrid material of V_2O_5 and rGO was able to achieve the theoretical capacity of 294.7 mAh g^{-1} at C/9 and, unlike the present material, lost less capacity as the current rate increased.[18] The capacity of at 1C step is 81% of the capacity of that at the C/9 step in comparison to the featured 220 ˚C annealing condition which only retained 56% of its peak capacity when the current rate was increased.[18] This hints that the mesoporous electrode in literature possesses higher stability at higher applied currents.[18] The discrepancy in stability could be due to either the difference in hydration within the two materials or the weight percentage of rGO within the hybrid material. In the case of two lithium insertion both the material annealed at 220 and 350 ˚C have similar quantities of rGO (I_G/I_D ratios of 1.26 vs 1.33) but different degrees of hydration (n = 0.76 vs 0.35) and show similar rate performance indicating that degree of hydration played little role in this instance. When comparing the 220 and 350 ˚C annealed conditions, the condition annealed at 220 ˚C out preforms the later in terms of stability and capacity retention when increasing the current rate. It is noted that the 220 ˚C annealed condition has over double weight percentage of the rGO (17 wt% vs 7 wt%). One big difference between the 220 ˚C annealed condition and the mesoporous V_2O_5 hybrid in literature is the wt% of rGO. The 220 ˚C annealed condition has roughly 17 wt% rGO comparing to the literature which

has roughly 30 wt% rGO. When looking at the 3-lithium insertion, one example in literature focuses on V_2O_5 deposited on vertically aligned carbon nanofibers.[3] The material deposited on the vertically aligned nanofibers was able to achieve a capacity of 500 mAh g^{-1} at C/3.5 rate in comparison to the 350 ˚C annealed condition which gives capacity of 440 mAh g^{-1} at C/9, matching the theoretical capacity for 3 lithium insertion.[2] The VACNF hybrid material also shows less capacity loss when increasing the applied current rate.[2] This is most likely due to the much-reduced lithium ion diffusion distance due to the unique morphology of the material that dramatically decreases the diffusion distance.. One way to improve the electrode stability would be to anneal the hybrid material in such a way to minimize carbon loss. This could be done via annealing using an inert gas or in a vacuum oven.

Magnesium Ion Electrochemical Characterization

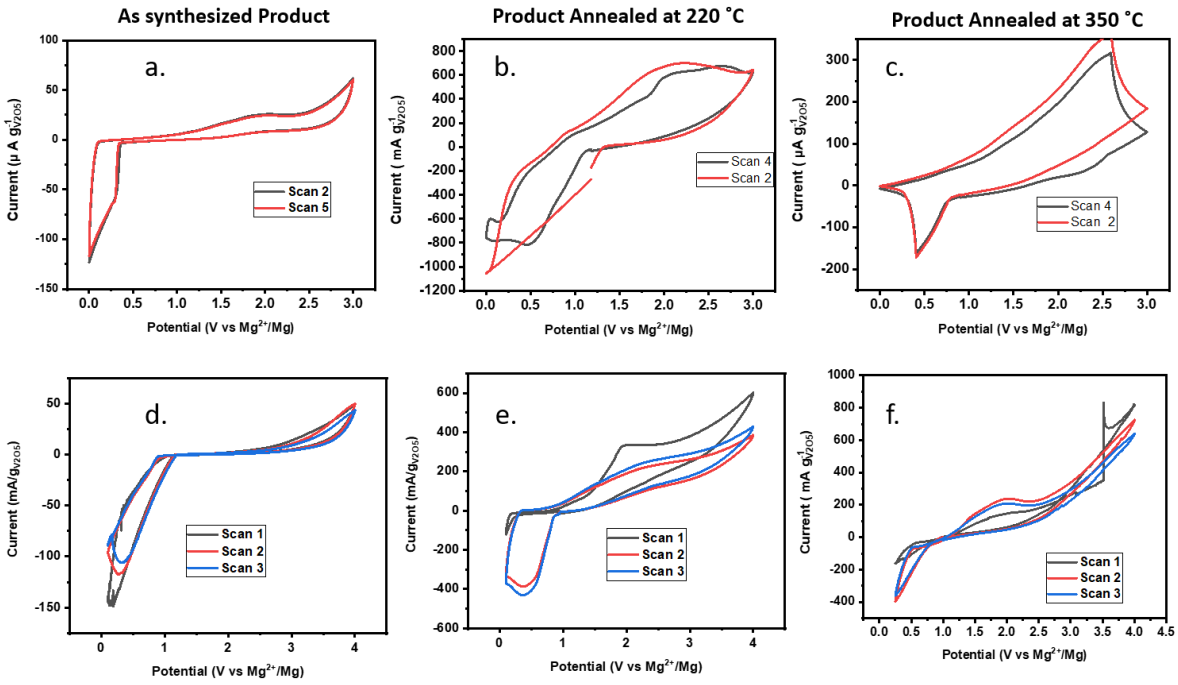

Figure 10. (a-c) Cyclic voltammograms of the three conditions utilizing a mechanically polished magnesium counter electrode at a scan rate of 1mV/s. (d-f) Cyclic voltammograms of the three conditions utilizing a SEI treated magnesium counter electrode at a scan rate of 1mV/s.

Figures 10a-c shows cyclic voltammograms (CV) of V_2O_5-rGO versus Mg anode at a scan rate of 1 mV/s, with 5 continuous cycles, respectively. Figures 10d-f show cyclic voltammograms of the same conditions, but with the addition of an engineered lithium solid electrolyte interface (SEI) on the magnesium anode. The lithium SEI treatment was applied because magnesium anodes often develop a compact Mg SEI layer in Mg-ion batteries which is not permeable to Mg^{2+} ions, hampering the reversibility and long-term stability of magnesium ion cells. However, a lithium SEI layer was found in literature to enable the passage of magnesium ions.[10, 24] The CVs of the cathodes made of the V_2O_5-rGO at each annealing conditions look fairly different from each other which are likely related to changes in hydration and crystallinity of the material as the annealing

temperature increases. None of the cyclic voltammograms represent typical battery behavior. In addition to this, in all cases there is high peak separation between the oxidation and reduction peaks indicating that all conditions are beset by low magnesium reversibility. However, this behavior and high peak seperation[8, 12, 25, 26] from all figures are typical in many magnesium ion batteries in literature. Incorporating a lithium SEI layer in all conditions has widened the application potential range from 0-3 V to 0.1- 4 V. The results of the normal Mg-ion battery with as-synthesized V_2O_5-rGO cathode in Figure 10a show s small oxidation peak at 2.0 V and a reduction peak below 0.25 V with a high peak separation, as commonly observed in magnesium ion batteries. The high over potential could be due to the formation of an insulating Mg SEI layer at the magnesium acetate/magnesium electrode interface in comparison to the cell protected by a pre-coated Li SEI in Figure 10d. The 220 ˚C annealing condition in Figure 10b shows an oxidation peak and reduction peak at 2.04 and 0.498 V, respectively. The sample annealed 350 ˚C in Figure 10c has a pair of oxidation and reduction peaks at 2.51 and 0.402 V, while the sample with a pre-coated Li SEI shows an oxidation peak at lower potential (~1.9 V) and a continuously increase reduction peak below 0.75 V. When considering the effect of hydration, the as-synthesized condition in both Figures 10a and 10e have the lowest magnitude of current per gram of V_2O_5, but it also contains the least conductive rGO among the three types of samples. The 220 ˚C annealed sample produced the double the degree of hydration compared to the 350 ˚C annealed condition (n = 0.76 vs 0.35) and gives a higher magnitude of current per gram of V_2O_5 in both the Li SEI protected and simply polished Mg anodes.

Figure 11a-c show the rate performance profiles of all conditions of the V_2O_5-rGO hybrid electrodes utilizing a magnesium anode. All referred C rates are based on the charge/discharge time relative to the standard rate of 1C. The specific capacity was calculated using the mass of

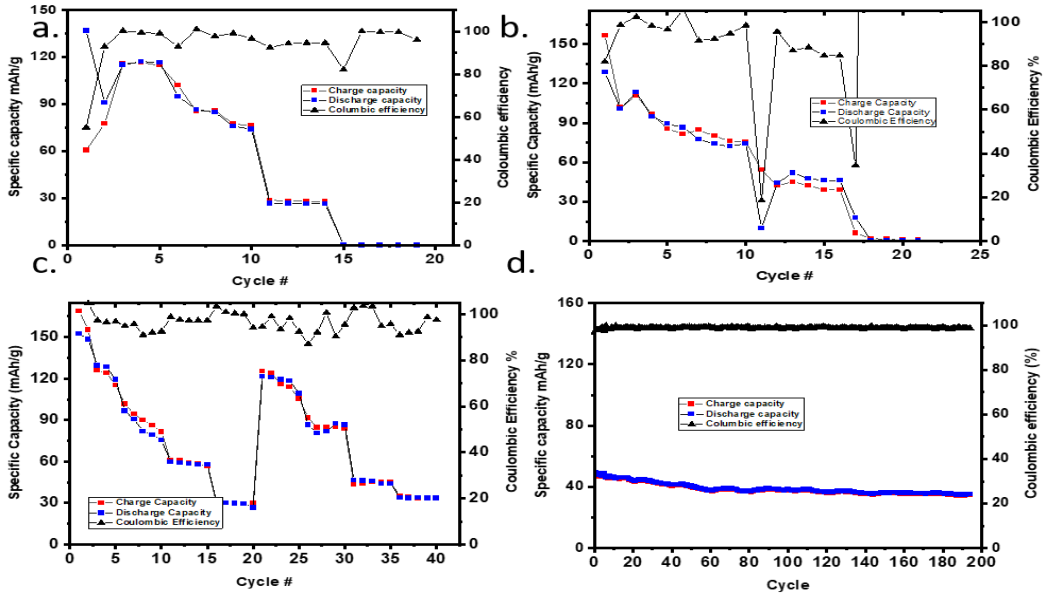

Figure 11.. (a-b) One rate performance sequence of the as-synthesized and 220 ˚C annealed samples using a mechanically polished magnesium anode at C/8, C/4, C/2 and 1C rates. (c) Two rate performance cycles of the 350 ˚C annealed sample using a mechanically polished magnesium anode at C/8, C/4, C/2 and 1C rates. (Current densities: 40,80, 160, 320 A g^{-1}) (d) A long cycling measurement of the 350 ˚C annealed sample using a polished magnesium electrode at C/2.

coated V_2O_5 for all three present conditions varied from ~72% to 94% depending on the degree of hydration, based on the TGA study discussed earlier. For the as-synthesized condition, the insertion and extraction capacities reach 140 mAh g^{-1} and 60 mAh g^{-1} respectively with the coulombic efficiency of ~40% during the first cycle at C/8. However, the coulombic efficiency improved even as the capacity widely varied during the C/8 rate. The average specific capacity of the as-synthesized condition at C/8 rate is 120 mAh g^{-1}, much lower than the theoretical capacity of 294.7 mAh g^{-1}. Both the capacity and coulombic efficiency have either declined sharply or varied in the charge-discharge processes at the C/8 and C/4 rates. The capacity stabilized as the C

rate increased to C/2, but the capacity decreased drastically to 28 mAh g^{-1}. As the C-rate rose to C, the capacity decreased further to 0.2 mAh g^{-1}. This low stability and capacity at low applied currents could be due to the poor permeability of the Mg SEI layer at the anode. The 220 ˚C condition in Figure 11b showed a very similar trend, possessing a higher initial capacity of 150 mAh g^{-1} and a higher specific capacity at 45 mAh g^{-1} at C/2 rate. In both cases, once the C-rate is increased to 1C, the capacity falls to nearly 0. The 350 ˚C annealed sample showed an even higher initial capacity of 165 mAh g^{-1} at C/8. However, the behavior at C/8 and C/4 rates are very similar to the other two conditions, displaying a fluctuating coulombic efficiency. Unlike the other two conditions, the 350 ˚C annealed sample showed fairly stable long-cycling performance at the high rate of C/2, able to retain 90% of its peak capacity (40 mAh g^{-1}) over 200 cycles with the columbic efficiency near 100% as shown in Figure 11d. The specific capacity also dropped less severely compared to the other two conditions as the C-rate is increased. The high crystallization of the 350 ˚C condition clearly improved the stable cycling at high current rates.

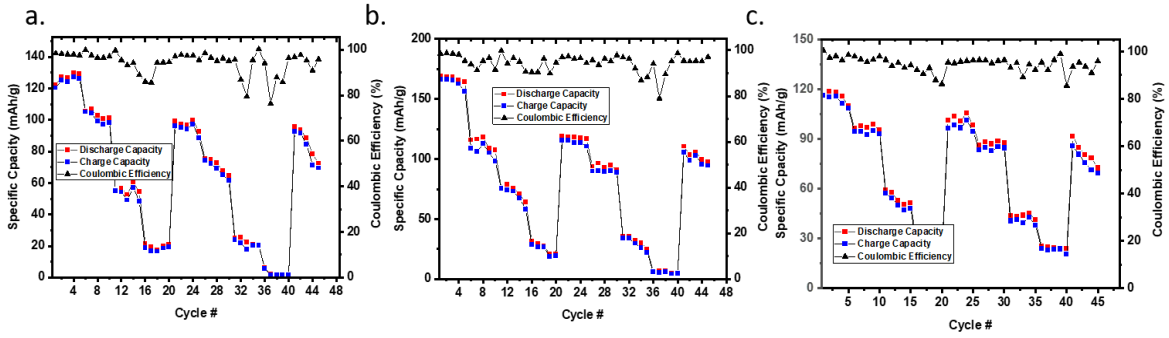

Figure 12. (a-c) Three rate performance cycles of the As-synthesized, 220, and 350 ˚C annealed condition using a SEI treated magnesium counter electrode at C/8, C/4, C/2, C.

Figures 12a-c show rate performance of the cell with the V_2O_5-rGO cathode prepared at the three conditions versus a pre-coated lithium SEI layer on the magnesium anode. In contrast to the cells utilizing the raw magnesium anode, the as-synthesized condition reached an initial capacity similar to the cell with the raw magnesium anode, but was far more stable and maintained

a consistent coulombic efficiency of 100% while as it reached a capacity of 135 mAh g^{-1} at C/8. The addition of a lithium SEI layer has increased the stability at the low current rates of C/4 and C/8. But as the C-rate was increased to 1C, the coulombic efficiency slid to 85% and the capacity decreased to 20 mAh g^{-1}. Once the second rate-sequence was commenced, the capacity recovered to 100 mAh g^{-1} at C/8. While this is better than the cell without pre-coated Li SEI, it is still only a 75% capacity recovery. The sample annealed at 220 ˚C behaved similarly to the as-synthesized condition, reaching a stable capacity of 170 mAh g^{-1} in the first C/8 rate while it maintained a coulombic efficiency near 100%. However, as the C-rate increased to C/4, C/2, and 1C, respectively, the coulombic efficiency varied from 90-95%. In the second rate-sequence, the capacity recovered to 80% of the prior C/8 step. Compared to the other two conditions, the product annealed at 350 ˚C showed a specific capacity similar to the as-synthesized condition, at all current steps. The condition annealed at 220 ˚C had the best overall cell performance much like in the 2-lithium insertion study, taking advantage of the high degree of both hydration and rGO.

Comparing to the current literature, the featured hybrid material suffered from a low capacity in the cell with native Mg SEI layer, giving only 0.576 moles of magnesium insertion per V_2O_5 corresponding to a capacity of 170 mAh g^{-1} at C/8.[8,10,11] In contrast, a study with graphene decorated V_2O_5 nanowires showed a capacity of 280 mAh g^{-1} at C/8, approximately 95% of the theoretical capacity.[11] In addition to its high capacity, this system was able to retain over 33% of its peak capacity when the applied current rate was increased to 1C.[11] The featured material retained only 15% of its peak capacity as the current rate was increased from C/8 to 1C. Compared to the 220 ˚C annealed product, the graphene decorated V_2O_5 possess a higher degree of hydration (1.42 vs 0,74 moles per V_2O_5).[11] The higher degree of hydration is likely beneficial to the battery performance. On the other hand, even though the as-synthesized product in this study has a similar

degree of hydration to the literature, it is limited by low electronic conductivity due to the fact that the carbon content is mostly GO, as revealed by the XRD, Raman and SAED spectra. Another limiting factor is the approximately 15% wt V^{4+} impurity which is much higher than the annealed conditions (~7%).

Improving the performance of the magnesium ion cell performance can go in three possible directions. The first involves altering the material synthesis to include more water within the reaction mixture. Water's higher tangent loss value means it will absorb more microwave radiation, enabling the reaction to achieve higher temperatures and pressures. This serves to increase the degree of hydration and to improve rGO quality, which will help to increase the shielding effects of H_2O while increasing the electronic conductivity of the rGO template. A second direction is to tackle the issue of the magnesium anode. As shown in Figure 12, covering the magnesium anode with a pre-coated lithium SEI layer can increase both the capacity and stability. While the cell performance decreased across multiple rate-performance cycles, it's possible that a thicker Li SEI layer would help.[8] The third possible direction for improvement is to use magnesium plated on a carbon template, preventing the creation of an insulating magnesium SEI layer.[8, 10]

Zinc Ion Electrochemical Characterization

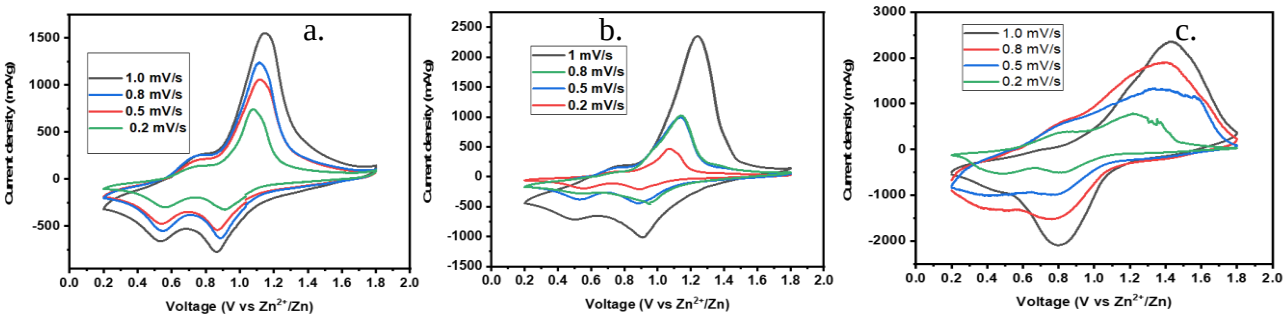

Figure 13. (a-c) Cyclic voltammograms of the V_2O_5-rGO electrode prepared at all three conditions in a zinc ion cell at 1, 0.8, 0.5, and 0.2 mV/s

Cyclic voltammetry (CV) measurements were performed to further investigate the V_2O_5-rGO hybrid electrodes for the Zn-ion storage. Figures 13a-c show representative CV curves of the V_2O_5-rGO materials prepared at previously described three conditions at diffident scan rates. The as-synthesized product showed two distinct pairs of peaks at around 0.58/0.75 V and 0.87/1.12 V (vs Zn^{2+}/Zn). This was attributed to a two-step reaction associated with Zn^{2+} ion intercalation and extraction. The 220 ˚**C** annealed condition showed two distinct pairs of peaks at 0.53/0.77 and 0.93/1.2 V. Furthermore, as the scan rate increased from 0.2 to 1 mV s^{-1}, the CV profiles retained their shapes, showing the good rate-performance of the V_2O_5-rGO cathodes. Importantly the CV measurements indicated that 0.2 to 1.8 V would be a proper operating potential range.

Figure 14a show the rate-performance profiles of the V_2O_5-rGO hybrid electrode at 4 different C-rates (C, 2C, 4C, and 8C) for 5 cycles each. While these rates are very high compared to Lithium-ion and Mg-ion batteries, they are common in literature on Zinc-ion batteries.[9, 27] The specific capacity was calculated using the mass of coated V_2O_5 for all three present conditions which vary from ~72-94% depending on the degree of hydration, based on the TGA study. The theoretical capacity for 1 mol of Zinc storage is 294.7 mAh g^{-1}. The as-synthesized sample gave capacities of 295, 250, 210 and 140 mAh g^{-1} at 1C, 2C, 4C, and 8C respectively, as the columbic

efficiency remained near 100% through all the rate performance steps. The observed capacity drop between applied current rates was less steep than in the lithium and magnesium cells. Upon the commencement of the second-rate performance step, the as-synthesized product achieved stable capacity of 325 mAh g^{-1} at C, when the current was reduced back to 1C after 20 cycles of rate tests, which was slightly more than its initial capacity. In the third 1C step (after 40 cycles), the capacity at rate 1C drops 275 mAh g^{-1}, retaining 77% of the peak capacity. The long cycling stability was further evaluated by charging–discharging the V_2O_5-rGO hybrid electrode at 1C for 400 cycles. Figure 14b revealed that this, and all conditions suffered from severe capacity loss. Specifically, the as-synthesized dropped from 335 mAh g^{-1} to approximately 50 mAh g^{-1}over the course of 400 cycles. One method to increase long term performance is to increase the applied current rate. Figure 14a show that the 4C (800 mA g^{-1}) step was more stable than the C (200 mA g^{-1}) step in all conditions. Figures 14c-e show that the increasing the applied current rate from C increased capacity retention. Figure 14c shows that when operating at 4C, the as-synthesized condition retained 50% of its peak capacity over 110 cycles. In that same time period, the as-synthesized condition retained only 21.6% of its capacity at 1C. The enhancement to stability came at a cost of capacity as the cell running at 4C only gave 200 mAh g^{-1} out of the theoretical capacity of 294.7 mAh g^{-1}.

Similar to Li-ion and Mg-ion batteries in earlier studies, the sample prepared at 220 ˚**C** showed the best performance. The 220 ˚C condition gave stable capacities of 400, 376, 345 and 305 mAh g^{-1} at 1C, 2C, 4C, and 8C, respectively. The columbic efficiency remained near 100% through all the rate-performance tests. The second C step of the 220 ˚C annealed sample recovered approximately 96% the peak capacity (395 mAh g^{-1} vs 410 mAh g^{-1}) of the first C step. After 40 cycles the third C step recovers only 81% of the first C-steps peak capacity. The 220 ˚C samples

ability to recover capacity when transitioning from high to low applied current rates is a good sign of electrode stability. The long cycling stability was further evaluated by charging–discharging the V_2O_5-rGO hybrid electrode at 1C for 400 cycles. The 220 ˚C sample, like the other two samples, showed a dramatic capacity loss over 400 cycles at C, retaining only 12% of its peak capacity. When operated at a higher current rate of 4C, the 220 ˚C product retained 55% of its capacity after 110 cycles, while it only retained 38% of its peak capacity at 1C during the same time period. The 220 ˚**C** annealed sample in Figure 14d showed a much higher peak capacity of 350 mAh g^{-1} at 4C, which exceeded the theoretical capacity by 36%. A similar trend is seen in the other two conditions.

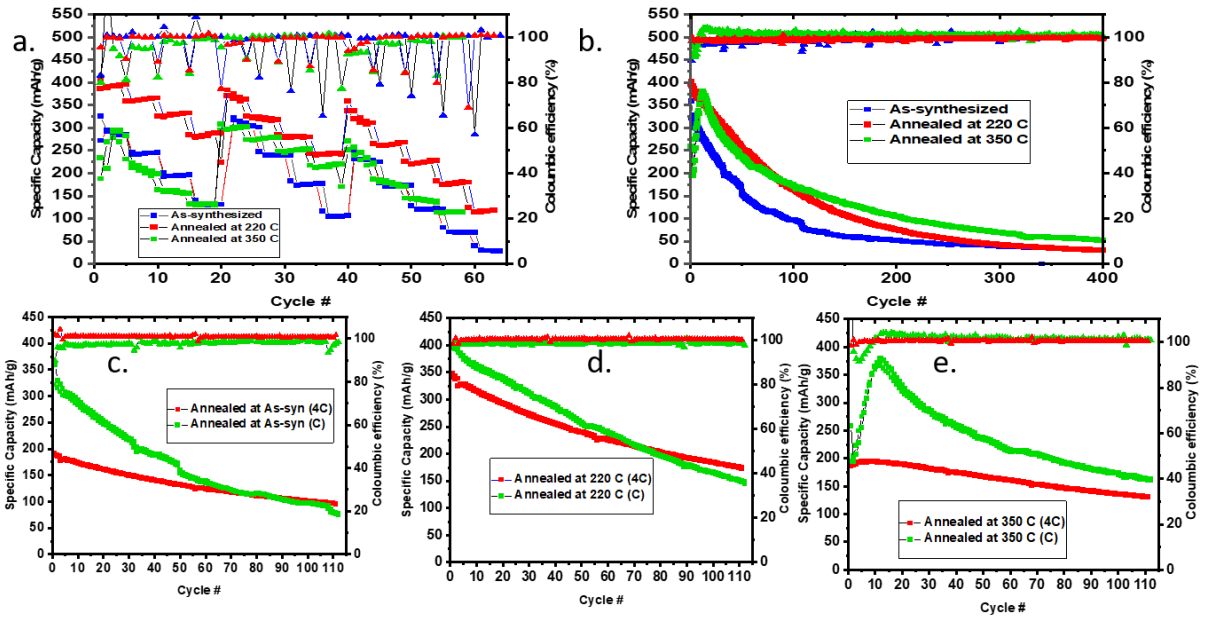

Figure 14. (a) Three rate performance cycles of the As-synthesized, 220 ˚C and 350 ˚C annealed samples versus a Zinc anode at C, 2C, 4C, 8C. (Current densities: 200,400, 800, 1600 mA g^{-1}) (b) Three long term cycling of the as-synthesized, 220 ˚C and 350 ˚C annealed samples versus a Zinc anode at 1C rate. (c-e) Three long cycling tests of the as-synthesized, 220 ˚C and 350 ˚C annealed samples versus a Zinc anode at 4C in comparison to 1C rates.

The 350 ˚C sample gave stable capacities of 300, 252, 176 and 150 mAh g^{-1} at 1C, 2C, 4C, and 8C, respectively. The columbic efficiency remained near 100% through all the rate-

performance tests. The second C step of the 350 ˚C annealed sample recovered approximately 110% the peak capacity (300 mAh g^{-1} vs 330 mAh g^{-1}) of the first C step. After 40 cycles the third C step recovers only 80% of the first C-steps peak capacity. The 350 ˚C samples ability to recover capacity when transitioning from high to low applied current rates is a good sign of electrode stability. The long cycling stability was further evaluated by charging–discharging the V_2O_5-rGO hybrid electrode at 1C for 400 cycles. While the initial capacity of the 350 ˚C sample grew to 375 mAh g^{-1} within the first 20 cycles, the sample lost 83% of its peak capacity over the course of 400 cycles. When operated at a higher current rate of 4C, the 350 ˚C sample retained 67% of its capacity after 110 cycles, while it only retained 43% of its peak capacity at 1C during the same time period.

The increased performance of the 220 ˚C annealed sample in comparison to the as-synthesized sample is due to the as synthesized sample possessing a much higher population of GO. A higher proportion of GO leaves the as-synthesized sample without the conductive and stabilizing impact of rGO. According to the materials characterization both annealed conditions possess more rGO than the as-synthesized condition. The 220 ˚C annealed sample also possess high interlayer spacing (12.1 Å). An advantage the sample annealed at 220 ˚C has over the product annealed at 350 ˚C is a higher interlayer spacing. The 350 ˚C annealed sample also lacks the shielding affects water due to its degree of hydration (n = 0.356 mols H_2O), and its low wt % of rGO (~7%).

Compared to literature, the featured material is able to achieve high capacity of 410 mAh g^{-1} at C. While this equates to 1.3 moles of inserted zinc, compared to literature, reversible capacities as high as 470 mAh g^{-1} have been reported at a similar applied current rate (C).[9] The featured material falters in terms of long term stability and high current rate performance. When using a high applied current rate (4C), the 220 ˚C annealed sample lost approximately half of its

peak capacity over the course of 110 cycles. In comparison a ball milled V_2O_5-graphite material retained over 90% of its peak capacity over 100 cycles at 4C.[9] Another material, a manganese doped hydrated V_2O_5 material, similarly held over 95% of its peak capacity over 200 cycles at a low applied current rate (C).[28] This material managed to achieve a peak capacity of 376 mAh g^{-1} at the lowest current rate C while retaining over 95% in both low and high applied current rates, something the featured material has struggled to do. This presents two possible paths forward for improvement; one involves utilizing a more concentrated electrolyte, while the second path involves introducing a manganese salt into the material. The authors reasoning for using a concentrated electrolyte 3 M $Zn(CF_3SO_3)_2$ instead of a "diluted" electrolyte 1 M $Zn(CF_3SO_3)_2$ is because the high-concentration electrolyte can decrease the water activity and water-induced side reactions that trap zinc ions within the electrode.[9] When comparing the two electrolyte concentrations in a long term stability test, the higher concentration electrolyte condition lost 5% of its peak capacity in over the span of 100 cycles while the lower concentration electrolyte condition lost 25% in that same time period.[9] Currently the zinc ion cell featured in this report utilizes 2M of Zinc perchlorate ($Zn(ClO_4)_2$) , so perhaps increasing the concentration to 3 or 4M may have the desired effect. A second path to possibly improving the zinc cell condition is by doping the hybrid material with manganese. The presence of manganese ions serves to both increase the interlayer spacing and reduces the bandgap, for example the Mn^{2+}-doped V_2O_5 narrows the bandgap of the material to 0.90 eV compared with that of pure V_2O_5 (2.28 eV) increasing the conductivity of the active material.[28] This could be applied to the featured material by adding manganese salt to the initial synthesis mixture.

Chapter 5 - Conclusion

In summary, the hybrid material based on V_2O_5 nanoparticles strongly anchored on rGO nanosheets have been successfully synthesized by using microwave synthesis vanadium(V) oxytriisopropoxide and GO. Further thermal annealing of the as-synthesized V_2O_5-rGO product at 220 ˚C and 350 ˚C respectively improved the quality of rGO, altered the morphology, and changed the degree of hydration. The as-synthesized material contained a sizable amount of GO in addition to the highest interlayer spacing, the largest V^{4+} impurity and degree of hydration. The sample annealed at 220 ˚C in air had a higher quality of rGO, while retaining its degree of hydration and high interlayer spacing, retaining its bilayer structure. The sample annealed at 350 ˚C in air had a similar quality of rGO while losing most of its hydration and interlayer spacing, becoming alpha crystalline V_2O_5. Unfortunately, the sample annealed at has the lowest wt % of carbon (7%).

When examining 2 lithium the product annealed at 220 ˚C came the closest to achieving theoretical capacity (295 mAh/g vs 294.7 mAh/g) at C/9. The sample annealed at 220 ˚C was also the most stable, maintaining a coulombic efficiency of ~100% and recovering ~95% of its peak capacity upon the commencement of a second-rate performance cycle. The 220 ˚C annealed product had the highest wt % of rGO (17%), enabling it to take the most advantage of rGO's properties as a conductive template. However, once 3 lithium insertion is tested the fully dehydrated sample annealed at 350 ˚C out preform the other two reaching its theoretical capacity of 440.4 mAh/g at C/9. While the 350 ˚C annealed condition is the most crystalline, it has the least hydration and % wt carbon content. The uniform more homogenously distributed orthorhombic crystals enabled three lithium ions to reversibly intercalate into the electrode while benefiting from the conductivity of rGO. An issue seen with the lithium ion cells and seen in subsequent zinc and magnesium conditions is that all have lacking electrode stability and high current performance

when compared to literature. A way to improve the lithium ion cells is to anneal the product using an inert gas or under vacuum in order to keep rGO weight percentage around 30% while the degree of hydration changes. Another possible means of improvement is to experiment with different carbon templates that could possibly decrease lithium ion diffusion distance.

When working with magnesium ion cells, all current conditions have issues with low capacity, achieving only ~55% of the theoretical capacity at best, and stability issues. The as-synthesized and 220 ˚C annealed samples both dramatically lost capacity both during their respective low c-rate performance step. While the capacity remains consistent at higher current rates, the capacity delivered is extremely low. The sample annealed at 350 ˚C behaved similarly to the other conditions except for stable cycling at the applied current rates of C/2 and C, maintaining a capacity of 40 mAh g^{-1} for 200 cycles. A reason for this poor performance is likely due to the organic electrolyte 1M Mg (ClO_4) in acetonitrile forming a passivating SEI layer that inhibited reversable magnesium ion diffusion.[10, 24] When altering the magnesium anode by applying a lithium SEI layer, performance across conditions improved. Specifically, the all three conditions were significantly more stable during the C/8 and C/4 steps possessing coulombic efficiencies near ~95%. Much like in the lithium cells, the 220 ˚C annealed sample had the highest capacity at 165 mAh g^{-1}at C/8. Despite the initial increased performance subsequent rate performance cycles show the capacity recovered to only ~70% of its current maxima, due to decreases in electrode stability. Given this, there are two paths to improve magnesium ion cells, the first if depositing a thicker lithium SEI layer of the magnesium anode, or using a carbon template plated with magnesium as a counter electrode. A second path to improving magnesium ion cells is to increase the degree of hydration and quality of rGO by adding more water to the initial reaction mixture.

When examining zinc ion battery performance, much like the lithium and treated SEI magnesium ion tests, the 220 ˚C annealed sample had the best performance, reaching the highest capacity reaching 410 mAh g^{-1} or about 1.37 moles of zinc insertion at C. This plus the high coulombic efficiency hovering near 100% indicate good electrode stability. However, the capacity failed to recover after two sets of rate performance cycles. Studying the long-term cycling at over 100 cycles shows that the capacity remained most stable at higher current rates, behaving similarly to the magnesium ion conditions, implying that better capacity at higher applied currents is characteristic of this material uses in divalent ion systems. However, all conditions of this material, even under high current rates, lost over a third of its peak capacity over 110 cycles. Compared to literature the zinc ion cells lack in long term stability and high current rate capacity. Tone possible path to improving zinc ion cells can be achieved by doping the hybrid material with manganese ions to increase the conductivity and interlayer spacing. Another path to improving the zinc ion cells is by using a more concentrated aqueous electrolyte which would inhibit water induced side reactions.

In summary, we report microwave hydrated V_2O_5-rGO as cathodes in next generation battery systems. Reported electrochemical performance can be attributed to three reasons. First, the rGO nanosheets enhance the materials conductivity, providing a better electrical pathway for electrons than V_2O_5 alone. Second, high interlayer spacing and water entombed within the structure shield ions to assist in diffusion. Third, a lower diffusion path length due to the high interlayer spacing and enhanced surface area by V_2O_5 nanoparticles. While the material is frequently capable of achieving its theoretical capacity, it suffers from long term electrode stability. Despite that the use of hydrated V_2O_5 deposited on a highly conductive and mechanically

stable rGO template via microwave radiation can serve as a foundation for future viable next gen battery materials.

Bibliography

1. Larcher, D.; Tarascon, J. M., Towards greener and more sustainable batteries for electrical energy storage. *Nature Chemistry* **2015,** *7* (1), 19-29.
2. Brown, J.; Li, J., Highly stable two and three lithium insertion in amorphous V2O5 shells coaxially deposited on electrospun carbon nanofibers: A self-supported membrane for high-capacity lithium ion battery cathodes. *Abstr Pap Am Chem S* **2018,** *255*.
3. Tarascon, J. M.; Armand, M., Issues and challenges facing rechargeable lithium batteries. *Nature* **2001,** *414* (6861), 359-367.
4. Van Noorden, R., The rechargeable revolution: A better battery. *Nature* **2014,** *507* (7490), 26-28.
5. Armand, M.; Tarascon, J. M., Building better batteries. *Nature* **2008,** *451* (7179), 652-657.
6. Canepa, P.; Sai Gautam, G.; Hannah, D. C.; Malik, R.; Liu, M.; Gallagher, K. G.; Persson, K. A.; Ceder, G., Odyssey of Multivalent Cathode Materials: Open Questions and Future Challenges. *Chemical Reviews* **2017,** *117* (5), 4287-4341.
7. Yao, J.; Li, Y.; Massé, R. C.; Uchaker, E.; Cao, G., Revitalized interest in vanadium pentoxide as cathode material for lithium-ion batteries and beyond. *Energy Storage Materials* **2018,** *11*, 205-259.
8. Huie, M. M.; Bock, D. C.; Takeuchi, E. S.; Marschilok, A. C.; Takeuchi, K. J., Cathode materials for magnesium and magnesium-ion based batteries. *Coordination Chemistry Reviews* **2015,** *287*, 15-27.
9. Xia, C.; Guo, J.; Lei, Y.; Liang, H.; Zhao, C.; Alshareef, H. N., Rechargeable Aqueous Zinc-Ion Battery Based on Porous Framework Zinc Pyrovanadate Intercalation Cathode. *Advanced Materials* **2018,** *30* (5), 1705580.
10. Tang, K.; Du, A.; Dong, S.; Cui, Z.; Liu, X.; Lu, C.; Zhao, J.; Zhou, X.; Cui, G., A Stable Solid Electrolyte Interphase for Magnesium Metal Anode Evolved from a Bulky Anion Lithium Salt. *Advanced Materials* **2020,** *32* (6), 1904987.
11. An, Q.; Li, Y.; Deog Yoo, H.; Chen, S.; Ru, Q.; Mai, L.; Yao, Y., Graphene decorated vanadium oxide nanowire aerogel for long-cycle-life magnesium battery cathodes. *Nano Energy* **2015,** *18*, 265-272.
12. Andrews, J. L.; Mukherjee, A.; Yoo, H. D.; Parija, A.; Marley, P. M.; Fakra, S.; Prendergast, D.; Cabana, J.; Klie, R. F.; Banerjee, S., Reversible Mg-Ion Insertion in a Metastable One-Dimensional Polymorph of V 2 O 5. *Chem* **2018**.
13. Clites, M.; Pomerantseva, E., Bilayered vanadium oxides by chemical pre-intercalation of alkali and alkali-earth ions as battery electrodes. *Energy Storage Materials* **2018,** *11*, 30-37.
14. Guex, L. G.; Sacchi, B.; Peuvot, K. F.; Andersson, R. L.; Pourrahimi, A. M.; Ström, V.; Farris, S.; Olsson, R. T., Experimental review: chemical reduction of graphene oxide (GO) to reduced graphene oxide (rGO) by aqueous chemistry. *Nanoscale* **2017,** *9* (27), 9562-9571.
15. Baghbanzadeh, M.; Carbone, L.; Cozzoli, P. D.; Kappe, C. O., Microwave-Assisted Synthesis of Colloidal Inorganic Nanocrystals. **2011,** *50* (48), 11312-11359.
16. Kilos, B.; Bell, A. T.; Iglesia, E., Mechanism and Site Requirements for Ethanol Oxidation on Vanadium Oxide Domains. *The Journal of Physical Chemistry C* **2009,** *113* (7), 2830-2836.

17. Paredes, J. I.; Villar-Rodil, S.; Martínez-Alonso, A.; Tascón, J. M. D., Graphene Oxide Dispersions in Organic Solvents. *Langmuir* **2008,** *24* (19), 10560-10564.
18. Pandey, G. P.; Liu, T.; Brown, E.; Yang, Y.; Li, Y.; Sun, X. S.; Fang, Y.; Li, J., Mesoporous Hybrids of Reduced Graphene Oxide and Vanadium Pentoxide for Enhanced Performance in Lithium-Ion Batteries and Electrochemical Capacitors. *ACS Applied Materials & Interfaces* **2016,** *8* (14), 9200-9210.
19. Wen, B.; Wang, X. X.; Cao, W. Q.; Shi, H. L.; Lu, M. M.; Wang, G.; Jin, H. B.; Wang, W. Z.; Yuan, J.; Cao, M. S., Reduced graphene oxides: the thinnest and most lightweight materials with highly efficient microwave attenuation performances of the carbon world. *Nanoscale* **2014,** *6* (11), 5754-5761.
20. Garino, N.; Sacco, A.; Castellino, M.; Muñoz-Tabares, J. A.; Chiodoni, A.; Agostino, V.; Margaria, V.; Gerosa, M.; Massaglia, G.; Quaglio, M., Microwave-Assisted Synthesis of Reduced Graphene Oxide/SnO2 Nanocomposite for Oxygen Reduction Reaction in Microbial Fuel Cells. *ACS Applied Materials & Interfaces* **2016,** *8* (7), 4633-4643.
21. Yan, J.; Wei, T.; Qiao, W.; Shao, B.; Zhao, Q.; Zhang, L.; Fan, Z., Rapid microwave-assisted synthesis of graphene nanosheet/Co3O4 composite for supercapacitors. *Electrochimica Acta* **2010,** *55* (23), 6973-6978.
22. Yang, J.; Jo, M. R.; Kang, M.; Huh, Y. S.; Jung, H.; Kang, Y.-M., Rapid and controllable synthesis of nitrogen doped reduced graphene oxide using microwave-assisted hydrothermal reaction for high power-density supercapacitors. *Carbon* **2014,** *73*, 106-113.
23. Hryha, E.; Rutqvist, E.; Nyborg, L., Stoichiometric vanadium oxides studied by XPS. *Surface and Interface Analysis* **2012,** *44* (8), 1022-1025.
24. Lv, R.; Guan, X.; Zhang, J.; Xia, Y.; Luo, J., Enabling Mg metal anodes rechargeable in conventional electrolytes by fast ionic transport interphase. *National Science Review* **2020,** *7* (2), 333-341.
25. Kaveevivitchai, W.; Jacobson, A. J., High Capacity Rechargeable Magnesium-Ion Batteries Based on a Microporous Molybdenum–Vanadium Oxide Cathode. *Chemistry of Materials* **2016,** *28* (13), 4593-4601.
26. Kim, D.-M.; Jung, S. C.; Ha, S.; Kim, Y.; Park, Y.; Ryu, J. H.; Han, Y.-K.; Lee, K. T., Cointercalation of Mg2+ Ions into Graphite for Magnesium-Ion Batteries. *Chemistry of Materials* **2018,** *30* (10), 3199-3203.
27. Yan, M.; He, P.; Chen, Y.; Wang, S.; Wei, Q.; Zhao, K.; Xu, X.; An, Q.; Shuang, Y.; Shao, Y.; Mueller, K. T.; Mai, L.; Liu, J.; Yang, J., Water-Lubricated Intercalation in V2 O5 ·nH2 O for High-Capacity and High-Rate Aqueous Rechargeable Zinc Batteries. *Advanced Materials* **2018,** *30* (1), 1703725.
28. Geng, H.; Cheng, M.; Wang, B.; Yang, Y.; Zhang, Y.; Li, C. C., Electronic Structure Regulation of Layered Vanadium Oxide via Interlayer Doping Strategy toward Superior High-Rate and Low-Temperature Zinc-Ion Batteries. *Advanced Functional Materials* **2019**, 1907684.
29. Holder, C. F.; Schaak, R. E., Tutorial on Powder X-ray Diffraction for Characterizing Nanoscale Materials. *ACS Nano* **2019,** *13* (7), 7359-7365.